nature communications

Article

https://doi.org/10.1038/s41467-025-67296-1

Atomic diffusion pathway mediated subsurface engineering

Received: 15 May 2025

Accepted: 26 November 2025

Published online: 13 December 2025

Check for updates

Xiaolin Tai[1,5], Yanan Zhou[2,5], Shilong Xu[3,5], Liuxin Xu[4], Hui Ding[1], Yan Xu[1], Renjie Gui[1], Xiao Han[1] ✉, Mingming Ma[1], Changzheng Wu[1] ✉ & Yue Lin[1] ✉

Subsurface regions critically govern surface events, such as the interactions with reactants in heterogeneous catalysis, thereby significantly modulating catalytic performance. However, precise control of subsurface atomic arrangement remains challenging due to complex metal-adsorbate interactions and limited structural accessibility. Here we achieve precise control of subsurface atomic layer in platinum-based intermetallic compounds through targeted positioning of heterometallic atoms to subsurface via in-situ constructed atomic diffusion pathways. This site-specific placement and subsequent thermodynamic-induced atomic rearrangement are governed by surface energy minimization and adsorbate-induced segregation. Through atomic-precision subsurface engineering, we successfully synthesize a series of $L1_0$ (face-centered tetragonal, fct)-PtFe@PtM_{sub}, where M_{sub} represents heteroatoms (Ru, Rh, Pd, Ag) incorporated into subsurface layers. As demonstrated, the as-synthesized $L1_0$-PtFe@$PtPd_{sub}$ simultaneously stabilizes ligand and strain effects, thereby breaking the trade-off in $L1_0$-PtM with Pt skin, where Pt skin typically quenches ligand effects while introducing strain effects. Consequently, $L1_0$-PtFe@$PtPd_{sub}$/C catalyst demonstrates practical proton exchange membrane fuel cells performance, simultaneously delivering high activity and durability. This work provides a rational strategy for catalyst design that promotes the understanding of subsurface active sites in heterogeneous catalysis.

The catalytic performance of a heterogeneous catalyst is predominantly determined by its surface and near-surface atomic architecture, which dictates both geometric configurations and electronic environments[1,2]. Surface modifications, including surface doping[3,4], small molecule functionalization[5–7], and surface encapsulation[8–10], are widely utilized to enhance catalytic performance in various industrial reactions[3,5,7,8]. However, surface structures directly involved in catalytic reactions frequently undergo irreversible reconstruction, leading to severe degradation of precisely engineered surface architectures[11–14]. Taking these into account, subsurface engineering has emerged as a robust alternative by leveraging electronically active yet structurally protected subsurface sites[2,15–17].

Subsurface engineering targets the manipulation of 2–3 atomic layers beneath a material's surface, which have been demonstrated to

[1]Hefei National Research Center for Physical Sciences at the Microscale, Key Laboratory of Precision and Intelligent Chemistry, School of Chemistry and Materials Science, University of Science and Technology of China, Hefei, Anhui, PR China. [2]School of Material Science and Chemical Engineering, Ningbo University, Ningbo, Zhejiang, PR China. [3]School of Materials and Chemical Engineering, Anhui Jianzhu University, Hefei, Anhui, PR China. [4]National Synchrotron Radiation Laboratory, University of Science and Technology of China, Hefei, Anhui, PR China. [5]These authors contributed equally: Xiaolin Tai, Yanan Zhou, Shilong Xu. ✉e-mail: xhan@ustc.edu.cn; czwu@ustc.edu.cn; linyue@ustc.edu.cn

play a critical role in surface events—particularly in heterogeneous catalysis—through strain and ligand effects[18]. Motivated by this promise, various strategies have been explored to regulate subsurface composition, including: (i) bottom-up construction in bulk model catalysts, such as chemical vapor deposition[19], electrodeposition[20], and molecular beam epitaxy (MBE)[15,21], (ii) in-situ incorporation of non-metallic species on catalysts under reaction conditions[22], exemplified by subsurface metal carburization[18]. Nevertheless, directly extending these bottom-up construction protocols, primarily for bulk materials, to nanocatalysts remains a challenge. Self-limited synthesis techniques, represented by atomic layer deposition (ALD), exhibit promising capabilities for the atomic-precision construction of subsurface in nanocatalysts[23,24]. However, the ALD synthesis technique suffers from limitations such as the lack of general applicability and challenges in achieving scalable batch fabrication[25]. Given these constraints, developing conventional wet-chemical synthesis methods—advantageous for their simplicity and scalability—to achieve the precise subsurface tailoring is urgently needed, while still hindered by embedded atomic sites and complex diffusion dynamics.

In this work, Pt-based intermetallic compounds (IMCs) featuring Pt skins integrate well-defined atomic structures and superior catalytic functionalities, providing an ideal platform for atomic-scale subsurface engineering and corresponding structure-activity relationship studies. We achieved atomic-precision subsurface engineering of $L1_0$-PtFe@Pt by targeted placement of heterometallic atoms via a simple liquid phase synthesis approach. This process involves in-situ construction of atomic diffusion pathways, followed by energy-minimized atomic rearrangement governed by surface thermodynamics and metal-adsorbate interaction. Based on this, we successfully synthesized $L1_0$-PtFe@PtM_{sub}, where M_{sub} represents in-situ incorporated subsurface heterometallic atoms, including Ru, Rh, Pd, and Ag. Specifically, these heteroatoms occupy the Fe vacancies generated via galvanic replacement and acid leaching[26,27], with subsequent atomic rearrangement stabilizing these subsurface sites. The as-synthesized $L1_0$-PtFe@$PtPd_{sub}$/C demonstrates that subsurface engineering stabilized ligand and strain effects, breaking ligand-strain effects trade-off—as the Pt-skin typically quenches spatially dependent ligand effect while generating strain effect. As a result, the $L1_0$-PtFe@$PtPd_{sub}$/C catalyst exhibits practical catalytic potential in proton exchange membrane fuel cells (PEMFCs), overcoming activity-durability trade-off in oxygen reduction reaction (ORR) through Pd_{sub} atoms modulating electronic environments of active sites on the surface and stabilizing metals against leaching. In a membrane electrode assembly (MEA), the $L1_0$-PtFe@$PtPd_{sub}$/C catalyst delivers a high initial mass activity (MA) of 1.17 A mg_{Pt}^{-1} at 0.9 V and a rated power density of 0.88 W cm^{-2}, surpassing that of commercial Pt/C. Moreover, it exhibits a MA retention of 88.1%, and a potential loss of only 15 mV at 0.8 A cm^{-2} and a rated power loss of 8% after 30,000 cycles of accelerated stress testing, exceeding the U.S. DOE 2025 technical targets.

Results and discussion

Subsurface atomic site modulation engineering

Highly ordered IMCs, characterized by a fully ordered heterogeneous atomic arrangement, have emerged as promising catalysts. Pt-based IMCs with Pt skin, possessing structural regularity, enable the implementation of a precise subsurface atomic regulation strategy. In this study, carbon-supported highly ordered $L1_0$-PtFe nanoparticles served as the initial templates. Subsurface lattice vacancies generated by the cooperative effects of galvanic replacement and acid leaching facilitate the in-situ incorporation of foreign metals[26,27]. Subsequent thermal-driven atomic diffusion and rearrangement enable the targeted incorporation of heteroatoms into the subsurface, ultimately leading to a stabilized subsurface structure (Fig. 1a).

To elucidate the underlying chemical mechanisms of subsurface engineering, we systematically investigated the incorporation behavior of various metals (Fig. 1b). The results reveal that the feasibility of incorporating foreign metals into the $L1_0$-PtFe nanoparticles is governed by the relative magnitudes of their reduction potentials

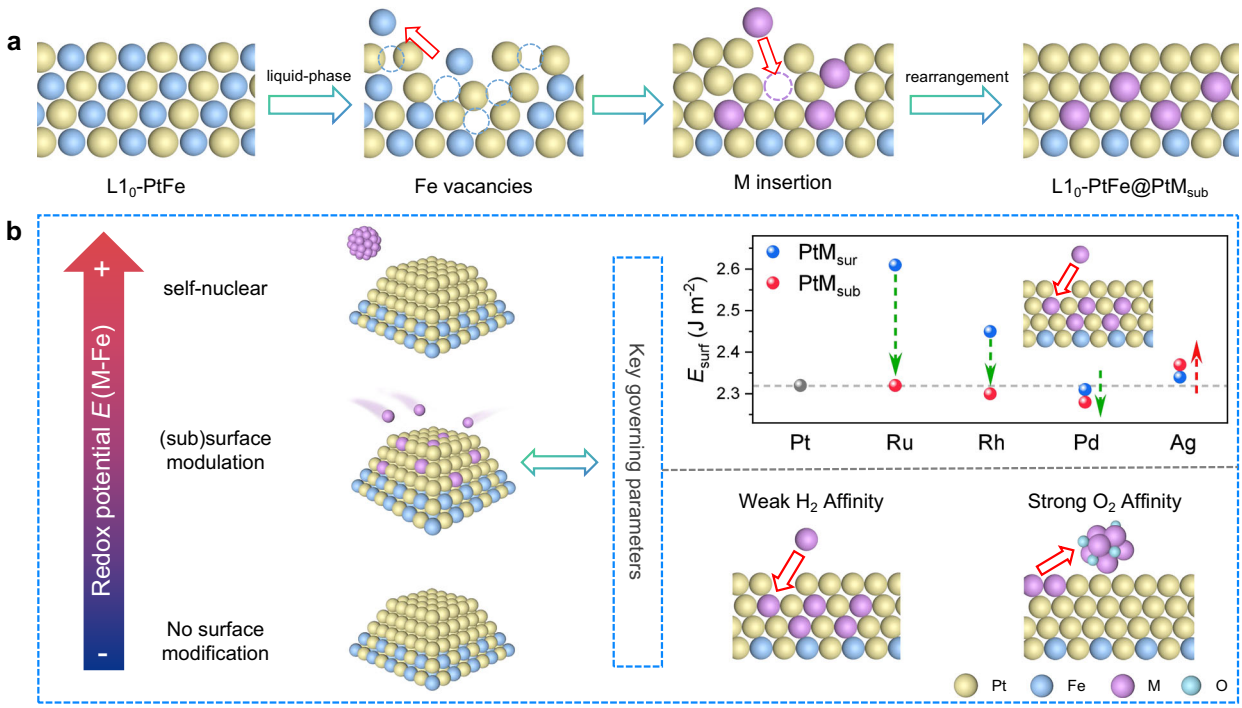

Fig. 1 | Subsurface atomic site modulation engineering. a Synthesis scheme for in-situ subsurface atomic site modulation strategy by conventional solution-phase synthesis. **b** Left: the redox potential-driven doping mechanism leads to selective doping, including self-nucleation, (sub)surface-modification, and no surface modification. Right: the lattice site occupancy of heterometallic atoms governed by key factors, including surface energy and metal-adsorbate interactions. The calculated surface energies of surface and subsurface sites were compared. Source data for the calculated surface energies are provided as a Source Data file.

($E_{M^{n+}}$/M) compared to that of Fe ($E_{Fe^{3+}}$/Fe)[28,29]. X-ray photoelectron spectroscopy (XPS) analysis confirms that the leached Fe species are primarily as Fe^{3+}, due to the weakly oxidizing acidic reaction conditions (Supplementary Fig. 1). For instance, 3*d* transition metals such as Zn, Co, and Ni, which exhibit lower redox potentials than Fe ($E_M < E_{Fe}$), are not incorporated into the nanoparticles due to their inability to replace Fe (lower-left in Fig. 1b). In contrast, metals with significantly higher redox potentials, such as Au, exhibit spontaneous nucleation and growth adjacent to the PtFe nanoparticles, rather than being integrated into the host structure (upper-left in Fig. 1b). To further investigate this behavior, we examined the elemental distribution of PtFe nanoparticles followed by Au introduction. The high-angle annular dark-field scanning transmission electron microscopy (HAADF-STEM) image and energy-dispersive X-ray spectroscopy (EDS) spectra reveal the formation of discrete, large nanoparticles with brighter contrast, which are predominantly composed of Au (Supplementary Fig. 2a, b). In contrast, the smaller PtFe nanoparticles show negligible Au content (Supplementary Fig. 2c). Furthermore, we systematically altered key reaction parameters—including lowering Au precursor concentration, reducing acid reaction temperature, and extending annealing—and found that Au invariably undergoes spontaneous nucleation and growth in all resulting samples (Supplementary Fig. 3). These observations confirm that Au tends to undergo spontaneous nucleation rather than incorporate into the PtFe lattice.

For other metals such as Mo, W, Ru, Rh, Pd, and Ag, which possess moderate redox potentials slightly higher than that of Fe, successful incorporation into the PtFe nanoparticles was achieved (center-left in Fig. 1b). The spatial distribution of these heteroatoms within the nanoparticles is subsequently governed by thermodynamic factors during the annealing process, particularly surface energy considerations and the metals' affinity for adsorbates (right in Fig. 1b)[30]. Among these, Mo and W exhibit the difficulty in reducing to metallic states and their strong affinities for oxygen[31,32], leading to the formation of Mo- and W-rich oxide clusters on the nanoparticle surface. As evidenced by HAADF-STEM images and EDS mappings (Supplementary Fig. 4), the intensity profiles of the mixed elemental mapping images show that Mo and W signals initiate further outward or overlap with Pt, confirming the surface localization of these oxide clusters. To understand the surface energy factor, we calculated the surface energy (E_{surf}) for various heterometals capable of incorporating into the host PtFe@Pt lattice. The E_{surf} for surface-alloyed (PtM_{sur}) and subsurface-alloyed (PtM_{sub}) configurations was compared to determine the preferential site occupancy of each element (right in Fig. 1b). The E_{surf} of pure Pt was determined to be 2.32 J m^{-2}. Upon alloying with Ru, Rh, and Pd, the E_{surf} of the corresponding PtM_{sur} structures were calculated to be 2.61, 2.45, and 2.31 J m^{-2}, respectively. Notably, these values are consistently higher than those of their subsurface-alloyed structures (2.32, 2.30, and 2.28 J m^{-2} for $PtRu_{sub}$, $PtRh_{sub}$, and $PtPd_{sub}$, respectively). These results strongly indicate that, from a thermodynamic perspective, the subsurface incorporation of Ru, Rh, and Pd confers greater structural stability[33]. Although Ag exhibits a lower E_{surf} in the surface-alloyed configuration (2.34 J m^{-2}) than that of $PtAg_{sub}$ configuration (2.37 J m^{-2}), its preferential migration to subsurface layers is ultimately driven by its weak interactions with hydrogen adsorbates under reductive annealing conditions. We summarize the redox potentials, calculated surface energies, and resulting doping behaviors of all heterometals in Table S2.

To experimentally confirm the distribution of M in the subsurface layer, we performed EDS elemental mapping and depth-resolved XPS to probe the surface and subsurface structures of PtFe@PtM_{sub} nanostructures. First, the nanoscale distribution of M was confirmed by HAADF-STEM and EDS elemental mapping, with the intensity profile of mixed elemental mapping revealing the presence of M peaks located between those of Pt and Fe (Fig. 2a–d). Moreover, the depth-resolved XPS was performed using photons-energy-dependent excitation (Fig. 2e–g). The Pt 4*f* and M 3*d* core-level signals were acquired under identical kinetic energy conditions, thereby maintaining a constant information depth. At a kinetic energy of 140 eV, corresponding to a surface-sensitive probing regime, distinct Pt signals were observed, while no discernible signals from the M elements (M = Ag, Pd, Rh) were detected. As the kinetic energy increased to 170, 270, 370, and 470 eV, resulting in a greater probing depth, the intensities of M 3*d* peaks increase progressively from the background level (Fig. 2e–g). Furthermore, the M atomic concentration quantified by XPS was normalized to the value obtained at a kinetic energy of 470 eV (set as unity) to analyze its depth-dependent variation. As shown in Fig. 2h, the resulting profile rises rapidly from zero and then remains constant, indicating that M is located exclusively in subsurface sites, with no distribution on the surface or in the core regions. For Ru_{sub}, due to significant overlap between the Ru $3d_{5/2}$ (280.2 eV) and C 1*s* (284.6 eV) peaks, and further compounded by the high C content and low Ru concentration in the $L1_0$-PtFe@PtRu/C, the strong C 1*s* signal obscured the Ru 3*d* region, precluding reliable quantification. Moreover, the Ru 3*p* signal was too weak to be detected. To address this limitation and further support our findings, we supplemented more STEM-EDS results on $L1_0$-PtFe@$PtRu_{sub}$ nanoparticles, thereby strengthening the overall robustness of the dataset (Supplementary Fig. 5). These results suggested that the M elements are predominantly located in the subsurface region.

The role of Fe vacancies in facilitating the subsurface migration of M elements was further investigated, with $L1_0$-PtFe@$PtPd_{sub}$ serving as a model system. Through controlling the acid etching time to modulate Fe vacancy density, we conducted extensive statistical analysis on a large ensemble of nanoparticles to investigate the heteroatom Pd content and its lattice site occupancy. The Fe vacancy density is quantitatively defined as the deviation from the ideal 1:1 stoichiometry of the $L1_0$-PtFe. Specifically, it is calculated as 50 at% minus the experimentally measured atomic percentage of Fe (at%) by STEM-EDS. Firstly, the EDS results reveal that Pd doping was unachievable in the absence of Fe vacancies (Supplementary Fig. 6a), confirming that the presence of Fe vacancies is an essential prerequisite for the incorporation of Pd atoms into the nanoparticles. As the Fe vacancy density increased, a positive correlation with the Pd incorporation efficiency was observed (Supplementary Fig. 6e). When Fe vacancies were confined exclusively to the nanoparticle surface, the insufficient vacancy concentration significantly reduced the kinetic driving force for inward diffusion, resulting in the preferential localization of Pd atoms within the outermost atomic layer (Supplementary Fig. 6b). Only when the Fe vacancy density was increased within approximately the first three surface layers, Pd could incorporate into subsurface sites (Supplementary Fig. 6c). In addition, it was observed that even with sufficient Fe vacancies, excessive Pd content could lead to the surface segregation of Pd atoms (Supplementary Fig. 6d). These results collectively demonstrate that sufficient Fe vacancy density is critical for enabling effective diffusion and subsequent stabilization of heterogeneous Pd atoms within subsurface layers.

In summary, we employed redox potential, surface energy, and metal-adsorbate interaction as key descriptors to systematically investigate the behavior of various heterometallic atoms during subsurface engineering. Guided by this understanding, we successfully synthesized $L1_0$-PtFe@PtM_{sub}, where M_{sub} represents the incorporation of foreign metals, including Ru, Rh, Pd, and Ag. We further extended this strategy to $L1_2$-Pt_3Fe nanoparticles, demonstrating its general applicability across different ordered phases by using representative heterometallic atoms such as spontaneously-nucleated Au, subsurface-incorporated Pd and Ag, and surface-decorated WOx (Supplementary Fig. 7). The successful implementation of this strategy in $L1_0$-PtFe and $L1_2$-Pt_3Fe demonstrates its general applicability and potential for expanding the range of metal systems, offering an

https://doi.org/10.1038/s41467-025-67296-1

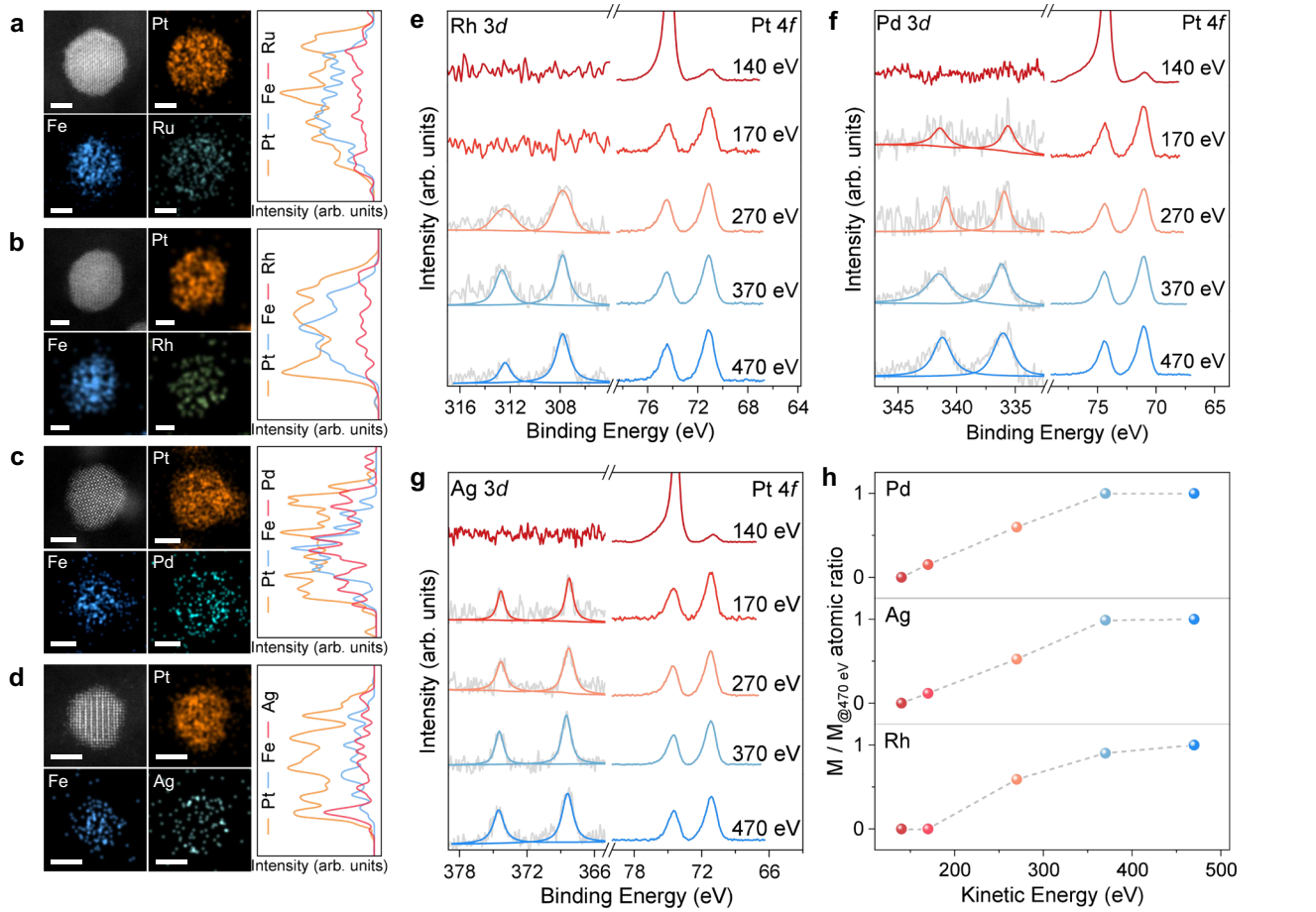

Fig. 2 | Subsurface atomic site modulation engineering. HAADF-STEM image and corresponding EDS mapping of individual $L1_0$-PtFe@PtRu NP (**a**), $L1_0$-PtFe@PtRh NP (**b**), $L1_0$-PtFe@PtPd NP (**c**), $L1_0$-PtFe@PtAg NP (**d**). The corresponding intensity profile of mixed-element mapping is shown to the right of the elemental mapping image. Scale bar, 2 nm. **e**–**g** XPS spectra of M 3*d*, Pt 4*f* in $L1_0$-PtFe@$PtRh_{sub}$/C, $L1_0$-PtFe@$PtRd_{sub}$/C, and $L1_0$-PtFe@$PtAg_{sub}$/C excited by photons with different energies. **h** Depth profile of M concentration in $L1_0$-PtFe@PtM_{sub}/C, with the concentration normalized to the value at a kinetic energy of 470 eV. Source data for the XPS are provided as a Source Data file.

efficient and versatile platform for precise modulation of the electronic environment at surface active sites.

Effects of subsurface engineering on structure

As a proof of concept, we demonstrated that subsurface engineering influenced the geometric and electronic structure of surface active sites and the practical catalytic potential of the $L1_0$-PtFe@$PtPd_{sub}$/C catalyst for the ORR in PEMFCs (Fig. 3a). As elaborated above, we constructed thermodynamically favorable subsurface $L1_0$-PtFe@$PtPd_{sub}$ configuration by incorporating Pd atoms into the in-situ generated Fe vacancies followed by thermal annealing. Furthermore, DFT calculations reveal a low kinetic barrier of 1.12 eV for the migration of surface Pd atoms into subsurface sites, which can be readily surmounted by our synthetic annealing conditions (Fig. 3b). The result indicates that the subsurface incorporation of Pd is kinetically accessible.

Following the initial experimental investigations, we conducted a detailed characterization of the microstructures of the $L1_0$-PtFe/C, $L1_0$-PtFe@Pt/C, and $L1_0$-PtFe@$PtPd_{sub}$/C catalysts. X-ray diffraction (XRD) patterns in Fig. 3c showed that the characteristic (001) and (110) peaks of the $L1_0$-PtFe/C, $L1_0$-PtFe@Pt/C, and $L1_0$-PtFe@$PtPd_{sub}$/C matched well with the ordered $L1_0$-PtFe intermetallic phase. The ordering degree of fresh $L1_0$-PtFe/C samples was calculated to be approximately 71.85%, determined by the ratio of the peak intensity of the (110) superlattice peak to the sum of the (111) and (200) peaks in XRD pattern[34], and neither acid-etching nor Pd_{sub}-doping treatments significantly reduced the ordering degree (Supplementary Fig. 8). Additionally, the as-synthesized $L1_0$-PtFe/C samples exhibited a uniform NP size distribution, as shown in the HAADF-STEM images (Supplementary Fig. 9). $L1_0$-PtFe@Pt and $L1_0$-PtFe@$PtPd_{sub}$ nanoparticles were uniformly dispersed on the carbon supports with an average particle size of approximately 3 nm, which is similar to that of the fresh $L1_0$-PtFe/C samples (Supplementary Figs. 10 and 11). In addition, atomic HAADF imaging revealed that the Pt and Fe atomic columns in the $L1_0$-PtFe are arranged in a periodic order (Supplementary Fig. 12). In the case of $L1_0$-PtFe@Pt, approximately three Pt layers covering the ordered intermetallic core can be observed (Supplementary Fig. 13). The HAADF-STEM image of the individual ordered PtFe@$PtPd_{sub}$ NP is viewed along the [100] zone axis and the corresponding fast Fourier transform pattern shows the presence of the (001) superlattice spots (Fig. 3c and Supplementary Fig. 14). Intensity profiles extracted from the shell layer reveal the presence of weaker intensity columns within the otherwise uniform intensity atom columns, suggesting that Pd atoms may occupy some Pt sites (Fig. 3d). Furthermore, EDS elemental mappings were conducted to analyze the elemental distribution of the as-synthesized catalysts (Supplementary Fig. 15–17). The composition of $L1_0$-PtFe/C, $L1_0$-PtFe@Pt/C and $L1_0$-PtFe@$PtPd_{sub}$/C was quantitatively analyzed by EDS, and the results were consistent with those obtained by inductively coupled plasma-mass spectrometry (ICP-MS), where the atomic ratio of Pt/Fe/Pd components was about 23:12.6:1 (Table S3).

https://doi.org/10.1038/s41467-025-67296-1

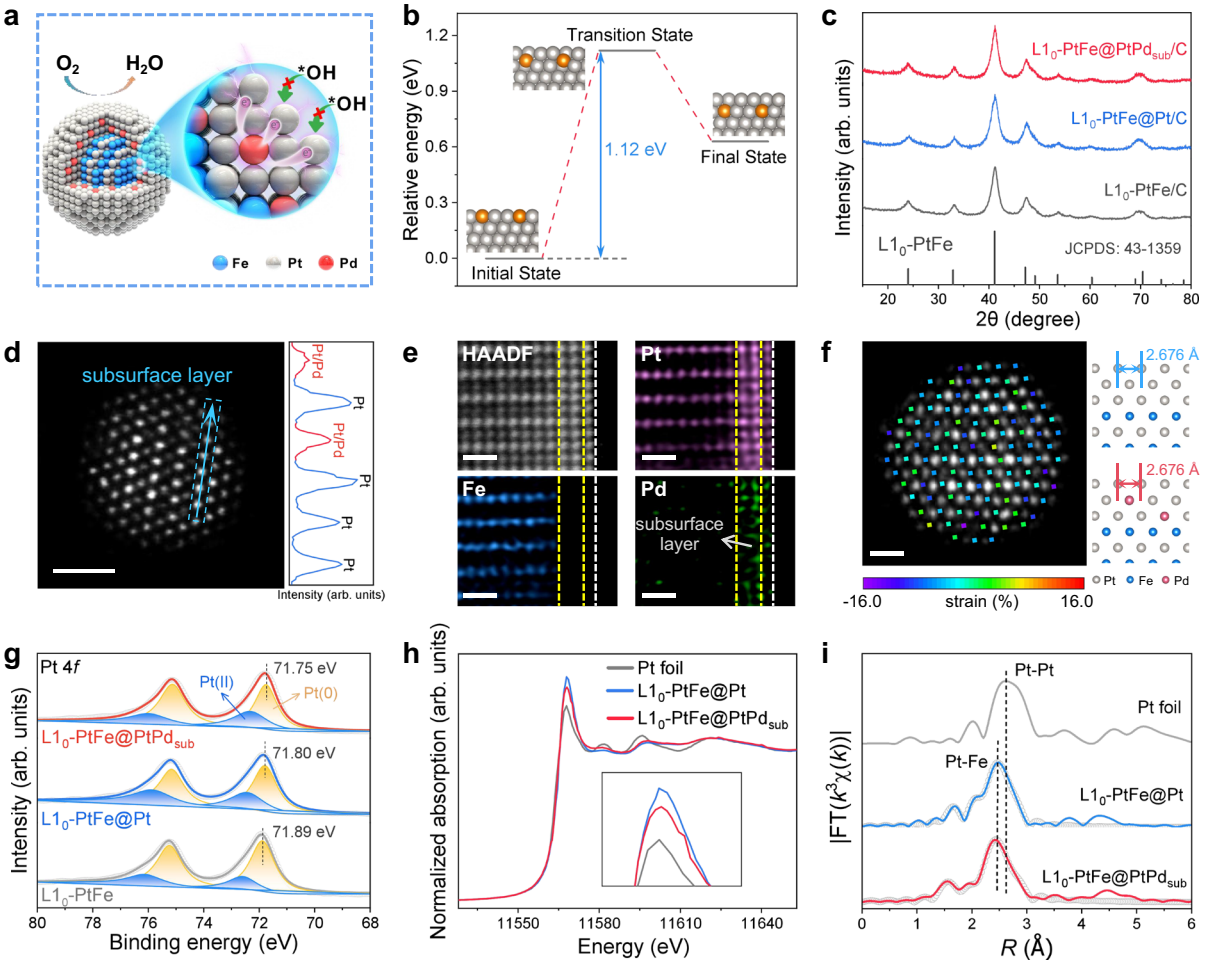

Fig. 3 | Phase and electronic structural characterization of subsurface engineering on $L1_0$-PtFe@Pt. a Schematic illustration of the subsurface atomic modulation strategy for $L1_0$-PtFe@$PtPd_{sub}$ nanocatalysts. **b** Calculated energy analysis of surface Pd atoms migrating into the subsurface layer. **c** XRD patterns of $L1_0$-PtFe/C, $L1_0$-PtFe@Pt/C, and $L1_0$-PtFe@$PtPd_{sub}$/C catalysts. The standard peaks of $L1_0$-PtFe are also shown. **d** Aberration-corrected HAADF-STEM image of a $L1_0$-PtFe@$PtPd_{sub}$ NP and the line profile of the marked region in the HAADF-STEM image. Scale bar, 1.0 nm. **e** HAADF-STEM image and corresponding atomic EDS elemental mapping of $L1_0$-PtFe@$PtPd_{sub}$ NP. Scale bar, 0.5 nm. **f** Enlarged and rotated view of (**d**) for clear visualization of the atomic strain analysis. scale bar, 0.5 nm. The colored squares correspond to different strain values. **g** Pt 4*f* XPS spectra of $L1_0$-PtFe/C, $L1_0$-PtFe@Pt/C, and $L1_0$-PtFe@$PtPd_{sub}$/C. **h** Pt L_3-edge XANES spectra of $L1_0$-PtFe@Pt/C, $L1_0$-PtFe@$PtPd_{sub}$/C, and Pt foil. **i** Fourier transformed X-ray absorption fine structure k^3-weighted $\chi(R)$ function spectra of $L1_0$-PtFe@Pt/C, $L1_0$-PtFe@$PtPd_{sub}$/C, and Pt foil. The dotted lines indicate the fitting results. Source data are provided as a Source Data file.

To investigate in detail the distribution of Pd atoms in the surface layer, we performed atomic elemental mapping. It is more intuitively apparent in the atomic-level EDS mappings that Pd is mainly located in the subsurface layer, which is also confirmed by EDS spectra acquired from the Pt shell and PtFe core regions (Fig. 3e and Supplementary Fig. 18). To further confirm the presence of Pd in the subsurface layer, we conducted CO-adsorption diffuse reflectance infrared Fourier transform spectroscopy (CO-DRIFTS) measurements. Since the carbon supports are black in color and exhibit strong light absorption, thus negatively impacting the signal-to-noise ratio and the accuracy of the results[35]. To address this issue, we replaced the carbon supports with light-colored irreducible supports, SBA-15, and confirmed the consistent structure of the $L1_0$-PtFe@Pt and $L1_0$-PtFe@$PtPd_{sub}$ nanoparticles on both supports by XRD and STEM measurements (Supplementary Figs. 19–22). There was one peak located at 2063 cm^{-1} on $L1_0$-PtFe@Pt/SBA-15 assigned to linear CO on Pt, which exhibited a slight red shift to 2062 cm^{-1} after incorporation of Pd, suggesting a modification in the electronic structure of Pt[36,37]. Notably, no new adsorption peaks emerged following Pd doping, indicating that the atomic structures of the surfaces of the two samples are comparable (Supplementary Fig. 23). In summary, Pd is predominantly located in the subsurface layer of the nanoparticles, which can be supported by experimental evidences.

Effects of subsurface engineering on electronic structure

Since the atomic radius of Pd is only marginally smaller than that of Pt (Pt: 139 pm, Pd: 137 pm), the strain alteration induced by the substitution of Pd for Pt sites should be minimal, which is proved by atomic-level strain analysis (Fig. 3f and Supplementary Fig. 24). The coordinate positions of each atomic column were determined using StatSTEM software[38], followed by measuring the spacing between the (110) planes. By comparing this spacing with the theoretical value for pure Pt, we derived the strain mapping image. Furthermore, XPS was conducted to analyze the electronic structure of the samples. As shown in Fig. 3g, the Pt $4f_{5/2}$ and Pt $4f_{7/2}$ spectra of $L1_0$-PtFe/C, $L1_0$-PtFe@Pt/C and $L1_0$-PtFe@$PtPd_{sub}$/C were deconstructed into two peaks assigned to Pt^0 and Pt^{2+}, with Pt^0 peak exhibiting larger peak area, indicating that Pt is predominantly in the metallic state. The binding energy of the Pt $4f_{7/2}$ peak in $L1_0$-PtFe/C (71.89 eV) is positively shifted by 0.10 eV compared to that of commercial Pt/C (71.79 eV), suggesting that the alloying between Pt and Fe has altered the electronic structure of Pt (Supplementary Fig. 25)[39]. Acid etching to form

https://doi.org/10.1038/s41467-025-67296-1

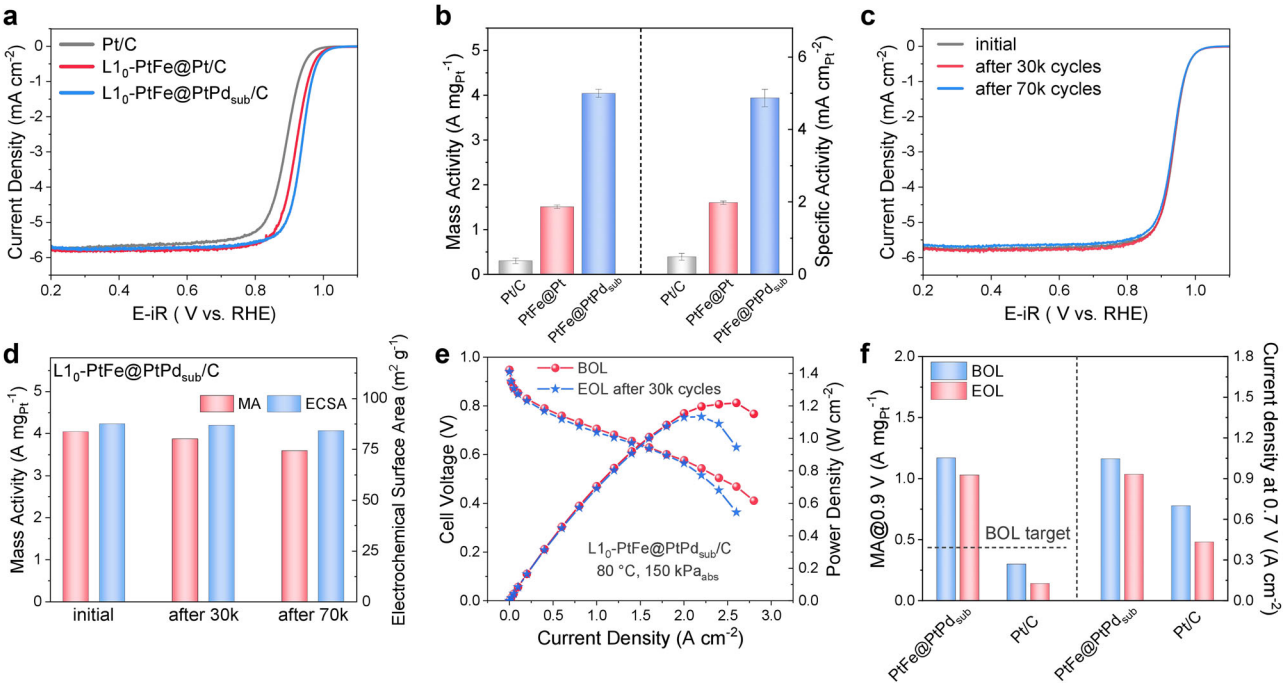

Fig. 4 | Electrocatalytic performance and MEA performance of L1$_0$-PtFe@PtPd$_{sub}$/C. a ORR polarization curve of L1$_0$-PtFe@Pt/C, L1$_0$-PtFe@PtPd$_{sub}$/C, and commercial Pt/C in O_2-saturated 0.1 M $HClO_4$ (pH = 1.01 ± 0.03; electrode surface area, 0.196 cm^2; rotating speed, 1600 rpm; scan rate, 10 mV s^{-1}). The iR was determined to be 19.7 ± 3.51 Ω. **b** MA and SA of the as-prepared catalysts at 0.9 V versus RHE. The error bars correspond to the standard deviation derived from five independent measurements. **c** ORR polarization curves of L1$_0$-PtFe@PtPd$_{sub}$/C in O_2-saturated 0.1 M $HClO_4$ (pH = 1.01 ± 0.03; electrode surface area, 0.196 cm^2; rotating speed, 1600 rpm; scan rate, 10 mV s^{-1}) before and after ADT. The iR was determined to be 19.7 ± 3.51 Ω. **d** The MA and ECSA of L1$_0$-PtFe@PtPd$_{sub}$/C before and after ADT. **e** H_2-air single-cell polarization curves and power density plots of the L1$_0$-PtFe/PtPd$_{sub}$ cathodes before (BOL) and after (EOL) AST test. Test conditions: cathode loading of 0.1 mg$_{Pt}$ cm^{-2}, 80 °C, 100% relative humidity, 150 kPa$_{abs}$. **f** MA at 0.9 V in H_2–O_2 fuel cells and the current density at 0.7 V in H_2-air fuel cells before and after AST test. Source data for the electrocatalytic performance data are provided as a Source Data file.

the Pt shell layer results in a negative shift of 0.09 eV in the binding energy of Pt 4$f_{7/2}$ compared to L1$_0$-PtFe/C. Additionally, the binding energy of the Pt 4$f_{7/2}$ peak in L1$_0$-PtFe@PtPd$_{sub}$/C (71.75 eV) exhibits a slight negative shift of 0.05 eV relative to that of L1$_0$-PtFe@Pt/C, proving that Pd$_{sub}$ effectively transfers electrons to Pt, thereby regulating the electronic environment of Pt. In X-ray absorption near-edge structure (XANES) spectra, the oxidation state of Pt can be determined by analyzing the white-line peak intensity at the Pt L_3-edge as it relates to the probability of electronic transition from the 2p orbital to the unoccupied 5d orbitals[40]. As shown in Fig. 3h, the white-line peak intensity of L1$_0$-PtFe@PtPd$_{sub}$/C is lower than that of L1$_0$-PtFe@Pt/C, indicating that the lower valence state of Pt is due to the extra electron transfer from Pd to Pt, in accordance with the XPS results. This indicates that the presence of Pd$_{sub}$ can alter the electronic structure of Pt, thereby exerting a ligand effect.

We further revealed the bonding information of the samples by analyzing the Fourier transforms extended X-ray absorption fine structure (FT-EXAFS)[41]. The FT-EXAFS spectra in R-space of Pt L_3-edge (Fig. 3i) show that the Pt-M coordination peaks of the samples are within the range of 2–3 Å. Compared to Pt foil, the Pt-Pt bond lengths of the studied catalysts were shortened by Pt-M (M = Fe, Pd) alloying, which could potentially enhance the ORR activity. Furthermore, the EXAFS spectra were subjected to a fit in order to infer local atomic coordination structural information (Fig. 3i and Supplementary Fig. 26). The Pt–Pt bond with an average coordination number of 5.7 in L1$_0$-PtFe@PtPd$_{sub}$/C exhibits a slight reduction in coordination compared to that of L1$_0$-PtFe@Pt/C (6.3), which confirms the successful doping of Pd$_{sub}$ (Table S4). The L1$_0$-PtFe@Pt/C and L1$_0$-PtFe@PtPd$_{sub}$/C exhibited similar peak positions corresponding to the Pt-M bonds, suggesting that the effect of Pd$_{sub}$ on the strain effect is negligible. The wavelet transforms of Pt L-edge EXAFS results in Supplementary Fig. 27 show that the k-space maxima of L1$_0$-PtFe@Pt/C and L1$_0$-PtFe@PtPd$_{sub}$/C are located at 7.0 Å^{-1} and 7.2 Å^{-1}, respectively, which are lower than that of the Pt foil (9.7 Å^{-1}), suggesting shortened Pt–M bonds in the studied catalysts. In addition, analysis of the Fe K-edge XAS data shows that the valence state and bond length of Fe remained unchanged (Supplementary Fig. 28). This indicates that the presence of Pd$_{sub}$ exerted minimal effect on the Fe within the core structure. These results suggest that the incorporation of subsurface Pd successfully modulates the electronic environment of Pt without affecting the original compressive strain.

ORR performance studies

The electrocatalytic performance of L1$_0$-PtFe@PtPd$_{sub}$/C catalyst for ORR was investigated by using rotating disk electrode (RDE) and MEA techniques. For comparison, undoped L1$_0$-PtFe@Pt/C and commercial Pt/C (20 wt%, TKK) were also tested under the same conditions for comparison. Figure 4a displays the RDE polarization curves of L1$_0$-PtFe@PtPd$_{sub}$/C, L1$_0$-PtFe@Pt/C and commercial Pt/C catalysts in O_2-saturated 0.1 M $HClO_4$ solution. Among these catalysts, L1$_0$-PtFe@PtPd$_{sub}$/C exhibited the most positive half-wave potential ($E_{1/2}$) of 0.94 V versus reversible hydrogen electrode (RHE). The MA of L1$_0$-PtFe@PtPd$_{sub}$/C at 0.9 V versus RHE was calculated to be 4.04 ± 0.17 A mg$_{Pt}^{-1}$, which is higher than 1.51 ± 0.04 A mg$_{Pt}^{-1}$ for L1$_0$-PtFe@Pt/C, and 0.30 ± 0.06 A mg$_{Pt}^{-1}$ for commercial Pt/C (Fig. 4b). The electrochemical surface areas (ECSAs) of the studied catalysts were quantified by the area of underpotential deposition of the hydrogen region (H_{UPD}). The specific activity (SA) of L1$_0$-PtFe@PtPd$_{sub}$/C, L1$_0$-PtFe@Pt/C, and commercial Pt/C catalysts was accordingly calculated to be 4.87 ± 0.24, 1.98 ± 0.05, and 0.48 ± 0.10 mA cm$_{Pt}^{-2}$, respectively (Fig. 4b). Among current research, there is a consensus that the performance of PtM@Pt is superior to that of Pt, which is attributed to the

https://doi.org/10.1038/s41467-025-67296-1

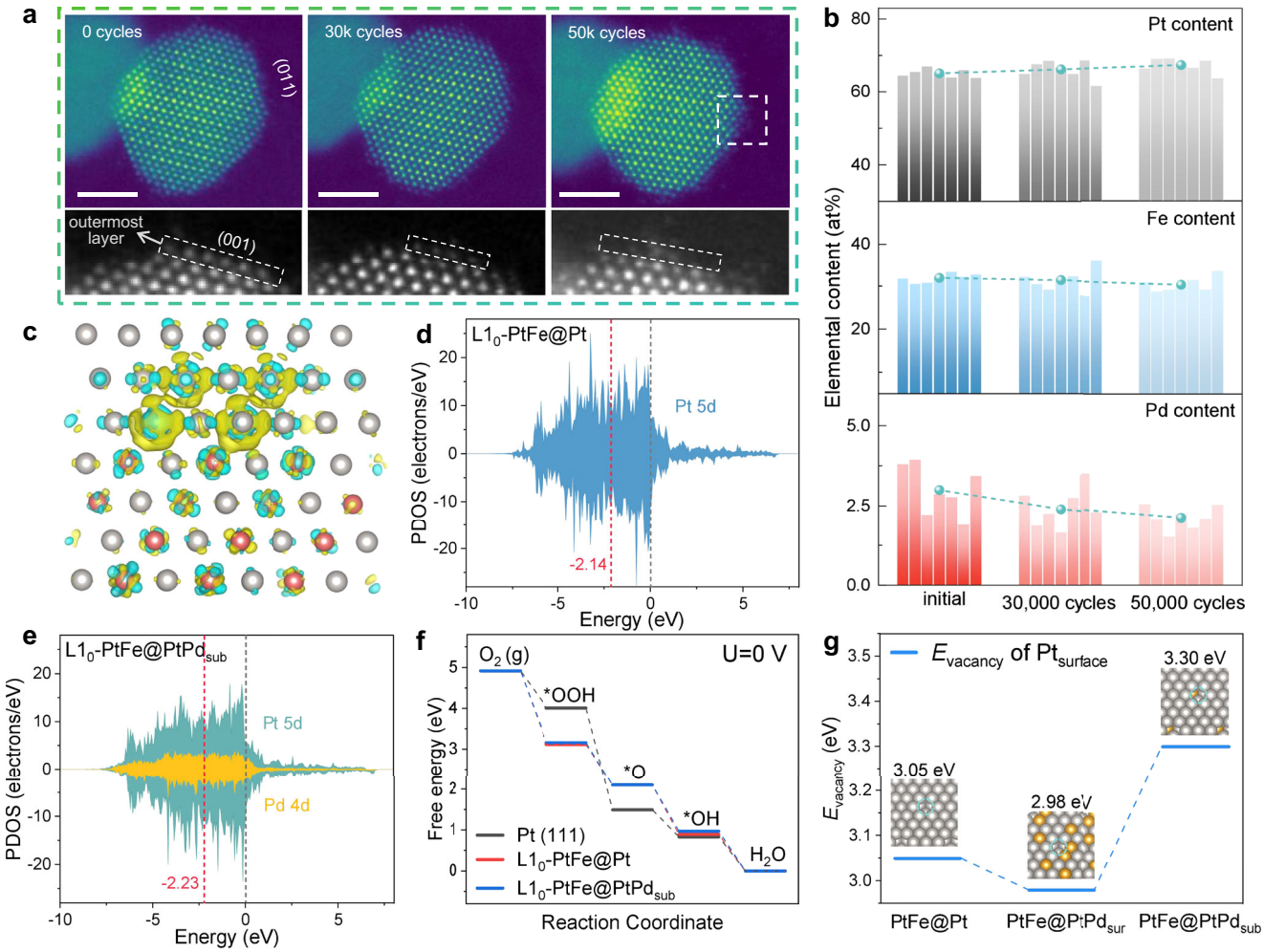

Fig. 5 | Identical location STEM (IL-STEM) results and mechanistic investigation. a IL-STEM images of $L1_0$-PtFe@PtPd$_{sub}$/C catalysts of initial, after 30,000 potential cycles, and after 50,000 potential cycles. Scale bar, 2 nm. **b** IL-EDS quantification of elemental content in catalysts at different reaction stages. **c** Charge density difference of $L1_0$-PtFe@PtPd$_{sub}$/C. The blue and yellow isosurfaces indicate charge accumulation and depletion, respectively. Gray spheres represent Pt atoms, and red spheres represent Pd atoms. **d** d-band PDOS (surface Pt layer) for $L1_0$-PtFe@Pt. **e** d-band PDOS (surface Pt layer and Pd 4*d*) for $L1_0$-PtFe@PtPd$_{sub}$. The Fermi level is set at zero energy (gray dashed line). **f** Calculated free energy diagram for $L1_0$-PtFe@PtPd$_{sub}$ (111), $L1_0$-PtFe@Pt (111), and Pt (111) catalysts under an electrode potential of 0 V. **g** Vacancy formation energy ($E_{vacancy}$) of surface Pt atoms for $L1_0$-PtFe@Pt, $L1_0$-PtFe@PtPd$_{sur}$, and $L1_0$-PtFe@PtPd$_{sub}$. Source data are provided as a Source Data file.

strain regulation[42]. Furthermore, the presence of Pd$_{sub}$ has nearly quadrupled the activity of $L1_0$-PtFe@PtPd$_{sub}$/C compared to $L1_0$-PtFe@Pt/C, strongly confirming that the ligand effect introduced by Pd$_{sub}$ significantly enhances ORR activity. Accelerated durability tests (ADTs) were conducted in O_2-saturated 0.1 M $HClO_4$ solution between 0.6 and 1.0 V versus RHE at a sweep rate of 100 mV s^{-1} to evaluate the durability of the catalysts. After 30,000 ADT cycles, $L1_0$-PtFe@Pt/C exhibited a significant loss of activity, with decreases of 21.85% in MA and 8.22% in ECSA (Supplementary Fig. 29). In contrast, $L1_0$-PtFe@PtPd$_{sub}$/C demonstrated markedly enhanced stability, retaining 95.79% of its MA and 99.21% of its ECSA after 30,000 ADT cycles. Remarkably, $L1_0$-PtFe@PtPd$_{sub}$/C maintained 88.86% of its initial MA and 96.11% of its initial ECSA even after 70,000 ADT cycles, highlighting its exceptional durability (Fig. 4c, d and Supplementary Fig. 30). Additionally, we conducted CO poisoning resistance tests on both samples, as this is a key metric of practical acidic ORR performance. The peak potential of CO stripping on $L1_0$-PtFe@PtPd$_{sub}$/C (852 mV) was smaller than that of $L1_0$-PtFe@Pt/C (881 mV) catalyst, verifying that $L1_0$-PtFe@PtPd$_{sub}$/C exhibited robust CO tolerance exceeding that of $L1_0$-PtFe@Pt/C (Supplementary Fig. 31). The introduction of subsurface Pd atoms on the $L1_0$-PtFe@Pt/C significantly enhances the ORR performance, which is attributed to the synergy of strain and ligand effects. Moreover, to confirm the observed enhancements indeed originate from the subsurface-specific effects rather than general Pd alloying effects, we synthesized a reference $L1_0$-PtFe@PtPd$_{sur}$/C catalyst with marginally increased Pd content, thereby allowing Pd to occupy not only subsurface but also surface sites (Supplementary Fig. 32). After 30,000 ADT cycles, this $L1_0$-PtFe@PtPd$_{sur}$ catalyst exhibited more pronounced performance degradation compared to the $L1_0$-PtFe@PtPd$_{sub}$ configuration (Supplementary Fig. 33). These experimental results strongly support the conclusion that the subsurface positioning of Pd plays a critical and distinct role in enhancing catalytic durability. Beyond this, we also evaluated the electrochemical performance of other $L1_0$-PtFe@PtM$_{sub}$/C catalysts (Supplementary Figs. 34–37). This finding provides a novel strategy for significantly enhancing the ORR activity and stability of Pt-based catalysts by regulating the subsurface atomic structure.

The $L1_0$-PtFe@PtPd$_{sub}$/C catalyst was used as a cathode catalyst layer for MEA and commercial Pt/C as the anode catalyst to evaluate the practical performance of as-prepared catalysts in PEMFCs. The cathodic and anodic catalytic layers of MEA were prepared by ultrasonic spraying with a Pt loading of 0.10 mg$_{Pt}$ cm^{-2} for the cathode and

0.05 mg_{Pt} cm^{-2} for the anode. A 30 wt% Pt/C (TKK) commercial cathode catalyst was tested under the same conditions for comparison. The intrinsic activity of the as-prepared catalysts was evaluated under H_2–O_2 conditions, where it was virtually unaffected by mass transport issues. Notably, the $L1_0$-PtFe@$PtPd_{sub}$/C catalyst achieved an initial MA value of 1.17 A mg_{Pt}^{-1} at 0.9 V, which is considerably higher than commercial Pt/C (0.3 A mg_{Pt}^{-1}) and the U.S. Department of Energy (DOE) 2025 target (0.44 A mg_{Pt}^{-1}) (Fig. 4f)[43]. The PEMFC performance of MEAs under H_2/air conditions was also investigated for practical applications. The peak power density of $L1_0$-PtFe@$PtPd_{sub}$/C catalyst reached 1.22 W cm^{-2} at a Pt loading of 0.10 mg_{Pt} cm^{-2}, which was significantly higher than that of the Pt/C catalyst (0.85 W cm^{-2}) (Fig. 4e and Supplementary Fig. 38). In addition, the current density of the $L1_0$-PtFe@$PtPd_{sub}$/C catalyst is considerably higher than that of commercial Pt/C catalyst within the typical operating voltage range (>0.6 V), in particular, a high current density of 1.05 A cm^{-2} can be achieved at 0.7 V. At the critical heat rejection limit, $L1_0$-PtFe@$PtPd_{sub}$/C cathode exhibited a rated power density of 1.26 W cm^{-2} at 0.67 V, performed at 94 °C and 250 kPa_{abs} (Supplementary Fig. 39). After being normalized to the total cathode Pt loading, the MEA made with $L1_0$-PtFe@$PtPd_{sub}$/C cathode showed an unprecedented Pt utilization efficiency of 0.079 g_{Pt} kW^{-1}, which surpassed the DOE 2025 target (<0.1 g_{PGM} kW^{-1}).

The durability of the as-prepared catalysts was evaluated by the accelerated stress test (AST) at 0.6 to 0.95 V under H_2/N_2 conditions. After 30,000 voltage cycles, the $L1_0$-PtFe@$PtPd_{sub}$/C catalyst retained 88.1% of the initial MA value, which is much higher than the 47% observed in commercial Pt/C catalyst (Fig. 4f). Notably, the end-of-life (EOL) MA (1.03 A mg_{Pt}^{-1}) was 3.96 times that of the DOE target value (0.26 A mg_{Pt}^{-1}) and 7.36 times the commercial Pt/C catalyst (0.14 A mg_{Pt}^{-1}). Furthermore, $L1_0$-PtFe@$PtPd_{sub}$/C also maintained a high EOL peak power of 1.14 W cm^{-2}, significantly outperforming most of the previously reported catalysts. Notably, the current density loss of $L1_0$-PtFe@$PtPd_{sub}$/C at 0.67 V is only 8.0%, and the voltage loss at 0.8 A cm^{-2} is about 15 mV, which is superior to Pt/C (72 mV) and also exceeds the DOE 2025 target of <30 mV. The $L1_0$-PtFe@$PtPd_{sub}$/C catalyst is one of the superior catalysts reported to date in terms of performance on many fuel cell metrics (Table S6). The above results confirm the high activity and structural stability of core-shell $L1_0$-PtFe@$PtPd_{sub}$/C catalyst under the conditions of practical PEMFC operation, demonstrating its prospects for practical application.

Identical location STEM characterization during ORR process

Structural reconstructions triggered by catalytic reactions are worth being investigated, as it provides valuable insights into the active sites of catalysts and guides the development of novel catalysts[44–46]. Identical location STEM (IL-STEM), as a quasi-in-situ technique, delivers high operational convenience and compatibility without any sacrifice in resolution[47,48]. In this study, we employed IL-STEM method to study the structural evolution of the $L1_0$-PtFe@$PtPd_{sub}$/C catalyst under ORR conditions. We first customized a working electrode capable of holding the TEM grid. After dropping the catalyst onto the TEM grid, it was then fixed onto the customized working electrode. At the desired reaction stage, the reaction is terminated and the grid can be removed from the electrode and observed using STEM, allowing for the examination of catalyst structural alterations in the same region, as shown in Supplementary Fig. 40. These operations can be repeated multiple times.

After 50,000 cycles of the ADT, the carbon support structure morphology and the pore structure changed slightly (Supplementary Figs. 41, 42). Additionally, the migration of NPs was noted, some of which were marked with blue circles (Supplementary Fig. 42). Furthermore, no disappearance of whole NPs due to dissolution was observed, and the formation of a limited number of clusters was observed (illustrated by orange circles), which should originate from the reassembly of single atoms dissolved from other particles. In addition, we investigated the atomic structure changes of the catalyst at the atomic scale (Fig. 5a). After 30,000 electrochemical potential cycles, the overall structure of the nanoparticles and the number of atomic layers remained almost unchanged, and the outermost layers of unsaturated coordination atoms were still present. The outermost layers exhibited only weak atomic dissolution and rearrangement, with very few single atoms observed at the periphery of the particle. After 50,000 potential cycles, the dissolution and rearrangement of the severely unsaturated coordinated atomic layers on the exposed (001) and (011) planes occurred, with preferential dissolution at the steps. This resulted in a reduction of two atomic layers on the (001) plane of the nanoparticle, while the number of atomic layers on the (011) plane remained unchanged. Additionally, clusters consisting of dispersed single atoms were observed in the vicinity. Some nanoparticles are somewhat amorphous on the Pt surface due to dissolution and rearrangement of atoms on the surface (Supplementary Fig. 43). However, the particle sizes remain unchanged, indicating that the nanoparticles have not undergone structural collapse. Additionally, the grain boundaries in nanoparticles remain unaffected following the reaction (Supplementary Fig. 43).

The changes in the elemental composition of $L1_0$-PtFe@$PtPd_{sub}$/C in the same region at different reaction cycles were quantitatively analyzed by EDS (Fig. 5b and Supplementary Fig. 41). We found that the changes in the composition of the Pt, Fe, and Pd on the $L1_0$-PtFe@$PtPd_{sub}$/C were insignificant, especially for Fe, which was barely dissolved. It is well established that the dissolution of non-precious metals in alloy catalysts is highly likely to occur, thereby accelerating the deactivation of the catalyst. For the $L1_0$-PtFe@Pt/C catalyst after 50,000 cycles, a similar phenomenon was observed, with the Fe content decreasing from 32.62 to 8.72 at.% (Supplementary Fig. 44 and Table S7). In contrast, for the $L1_0$-PtFe@$PtPd_{sub}$/C catalyst, the mitigation of Fe atom dissolution is proposed to arise from the presence of Pd_{sub}. The Pd_{sub} atoms greatly attenuate the structural collapse caused by surface Pt dissolution, thus preventing the formation of dissolution channels for Fe atoms. In addition, for the $L1_0$-PtFe@$PtPd_{sur}$/C catalyst with Pd on the surface, STEM-EDS mapping results of post-ADT catalysts revealed severe Pd leaching in multiple nanoparticles—contrast to the minimal Pd loss observed in the $L1_0$-PtFe@$PtPd_{sub}$/C catalyst (Supplementary Fig. 45). These results confirm that the enhanced stability originates specifically from the unique electronic and structural effects induced by the subsurface occupancy of Pd, which effectively mitigates metal dissolution and preserves the structural integrity.

Mechanistic investigation

DFT calculations were carried out to elucidate the effects of subsurface atomic modulation strategy on the electronic structures of surface active sites and the resulting ORR kinetics. Based on the information about the structural characterization of the catalysts, we constructed atomistic models of $L1_0$-PtFe@Pt, $L1_0$-PtFe@$PtPd_{sub}$, and Pt slab, and the optimized structures are shown in Supplementary Fig. 46. The charge density difference of $L1_0$-PtFe@$PtPd_{sub}$ catalyst in Fig. 5c reveals that electrons are transferred from Pd to Pt, where the blue and yellow isosurfaces indicate charge accumulation and depletion, respectively. In addition, Bader charge analysis showed that Pd lost 0.51 electrons, which further proved the effect of Pd on the surface Pt electronic structure, in alignment with the XAS results. This charge redistribution confirms that the incorporation of Pd effectively introduces ligand effects to the surface active sites. Furthermore, a comparison of the projected density of states (PDOS) between $L1_0$-PtFe@Pt (Fig. 5d) and $L1_0$-PtFe@$PtPd_{sub}$ reveals that the incorporation of Pd induces strong d-orbital hybridization between subsurface Pd and surface Pt atoms. This electronic interaction results in a downshift of the d-band center, from −2.14 eV in $L1_0$-PtFe@Pt to −2.23 eV in $L1_0$-PtFe@$PtPd_{sub}$, indicating a modulation of the surface electronic structure and weakened adsorption of oxygenated intermediates.

Given that the ORR reaction kinetics are closely related to the adsorption strength of the reaction intermediates on the Pt surface, we constructed models for the adsorption of different intermediate states in the four-electron associative ORR process (Supplementary Fig. 47). The computational hydrogen electrode (CHE) method was implemented to predict the free energy evolution along the four-electron ORR pathway on these catalysts when no external potential was applied ($U = 0$ V). The desorption kinetics of *OH intermediates is widely recognized as a key descriptor for catalytic performance in the ORR. The free energy diagrams in Fig. 5f indicate that the rate-determining step is the desorption of *OH for $L1_0$-PtFe@Pt and $L1_0$-PtFe@$PtPd_{sub}$, and the introduction of Pd can weaken the interaction between the *OH intermediate and catalysts, thereby accelerating the reaction. Notably, the compressive strain from the PtFe core alone weakens the *OH adsorption energy on the surface Pt sites by 0.06 eV compared to pure Pt. While this confirms a significant improvement over pure Pt, the incorporation of subsurface Pd in the PtFe@$PtPd_{sub}$ model further weakens the *OH adsorption energy by 0.08 eV. This comparison allows us to quantitatively decouple the strain effects from PtFe core and ligand effects from Pd atoms. The baseline strain effect counts for approximately 42.86% of the total weakening of *OH binding. The additional 57.14% improvement is directly attributable to the electronic effect induced by subsurface Pd, which provides a distinct benefit beyond pure lattice compression. This additional weakening of *OH binding by subsurface Pd is critical for optimizing the ORR activity. Moreover, given that Pt dissolution represents a major degradation pathway in electrocatalysts, the vacancy formation energy of surface Pt (E_{sur}) was calculated to evaluate the catalyst's stability. The E_{sur} values for $L1_0$-PtFe@Pt and $L1_0$-PtFe@$PtPd_{sub}$ were 3.05 and 3.30 eV, respectively, demonstrating that subsurface Pd atoms can inhibit Pt dissolution (Fig. 5g). In contrast, surface Pd lowers the E_{sur}, which may due to the higher dissolution tendency of Pd compared to Pt in acidic electrolytes. These results highlight the critical role of subsurface sites in stabilizing surface Pt. The theoretical insights support experimental findings, thereby providing additional evidence that the subsurface engineering strategy employed in $L1_0$-PtFe@Pt can effectively enhance ORR performance through combining ligand effects and compressive strain.

In summary, we developed a precise subsurface atomic modulation strategy through in-situ introducing foreign metal into the subsurface atomic layer, providing direct tuning of coordination and electronic structures. Guided by the principles of surface energy minimization and metal-adsorbate interactions, we successfully synthesized stabilized $L1_0$-PtFe@PtM_{sub} structures, M_{sub} represents in-situ incorporated heterometallic atoms, including Ru, Rh, Pd, and Ag. As a proof of concept, the as-synthesized $L1_0$-PtFe@$PtPd_{sub}$ simultaneously stabilizes ligand effects and maintains strain effects, thereby breaking the trade-off between ligand and strain effects in Pt-based IMCs with Pt skin. And the $L1_0$-PtFe@$PtPd_{sub}$ catalyst breaks the activity-durability trade-off in ORR, delivering practical fuel cell performance with both high activity and enhanced durability. The subsurface Pd atoms optimized the surface-intermediates interaction strength by modulating the surface electronic environments, while simultaneously suppressing the dissolution of metal atoms. This work presents an atomic-precision subsurface modulation strategy on tuning surface electronic structures of heterogeneous catalysts and opens new avenues for the development of novel catalysts.

Methods

Chemicals

Hexachloroplatinic hexahydrate ($H_2PtCl_6{\cdot}6H_2O$, AR), Iron(II) sulfate heptahydrate ($FeSO_4{\cdot}7H_2O$, AR, 99.0 ~ 101.0%), palladium(II) chloride ($PdCl_2$, AR), ruthenium(III) chloride hydrate ($RuCl_3{\cdot}xH_2O$, GR), rhodium(III) chloride hydrate ($RhCl_3{\cdot}xH_2O$, 98%), silver nitrate ($AgNO_3$, AR), tetrachloroauric(III) acid trihydrate ($HAuCl_4{\cdot}4H_2O$, AR, ≥47.8%), ammonium molybdate tetrahydrate ($Na_2MoO_4{\cdot}2H_2O$, AR, ≥99.0%), sodium tungsten oxide dihydrate ($Na_2WO_4{\cdot}2H_2O$, AR, ≥99.5%), and acetone (AR, ≥99.5%) were purchased from Sinopharm Chemical Reagent Co., Ltd (Shanghai, China). Perchloric acid (GR, 70.0–72.0% HClO4) was purchased from Sigma-Aldrich. Ketjenblack EC-600J carbon black was purchased from *Cabot*. All chemicals were used as received without further purification. Deionized (DI) water from Milli-Q System (Millipore, Billerica, MA) was used in all our experiments.

Synthesis of the $L1_0$-PtFe/C and $L1_0$-PtFe@Pt/C catalysts

Carbon-supported $L1_0$-PtFe IMCs catalysts were prepared by a wet-impregnation method. Specifically, 0.03 mmol $H_2PtCl_6{\cdot}6H_2O$ and 0.03 mmol $FeSO_4{\cdot}6H_2O$ were first dissolved in 20 mL of acetone, followed by the addition of 36 mg of Ketjenblack EC-600J. The mixture was stirred for 12 h to obtain a homogeneous solution, and then dried naturally at 25 °C. Finally, the dried powder was annealed in a tube furnace to 900 °C at 5 °C/min in an H_2/Ar (5:95) atmosphere and maintained for 2 h and then cooled to 25 °C to obtain $L1_0$-PtFe/C. To synthesize $L1_0$-PtFe@Pt/C, 10 mg $L1_0$-PtFe/C powder was dispersed in 15 mL of a 0.1 M $HClO_4$ solution, stirred and heated to 60 °C for 12 h. Then the solution was centrifuged, washed three times with DI water, and dried to obtain the powder, and the powder was annealed in a tube furnace to 400 °C at 5 °C/min in an H_2/Ar (5:95) atmosphere and maintained for 2 h.

Synthesis of the $L1_0$-PtFe@PtM_{sub}/C catalysts

The synthesis process of $L1_0$-PtFe@PtM_{sub}/C was demonstrated using $L1_0$-PtFe@$PtPd_{sub}$/C as an example. Specifically, 10 mg $L1_0$-PtFe/C powder was dispersed in 15 mL of a 0.1 M $HClO_4$ solution and subjected to ultrasonic treatment to form a homogeneous suspension. Subsequently, an aqueous solution of $PdCl_2$ (0.038 mg) was added, and the mixture was stirred and heated at 60 °C for 12 h. After the reaction, the solution was centrifuged, washed three times with DI water, and dried to obtain the final powder. Finally, the powder was annealed in a tube furnace to 400 °C at 5 °C/min in an H_2/Ar (5:95) atmosphere and maintained for 2 h. The synthesis of $L1_0$-PtFe@PtM_{sub}/C followed the same procedure as $L1_0$-PtFe@$PtPd_{sub}$/C, except that the $PdCl_2$ precursor was substituted with an equimolar amount of the M precursor, including $RuCl_3{\cdot}xH_2O$, $RhCl_3{\cdot}xH_2O$, $AgNO_3$, $HAuCl_4{\cdot}4H_2O$, $Na_2MoO_4{\cdot}2H_2O$, and $Na_2WO_4{\cdot}2H_2O$.

Structural characterizations

XRD patterns of as-prepared catalysts were examined using Philips X'Pert Pro Super diffractometer with Cu Kα radiation ($\lambda = 1.54178$ Å). Low magnification high-angle annular dark-field scanning transmission electron microscopy (HAADF-STEM) images and EDS mapping were carried out on the Thermo Fisher Talos F200X with the Super X-EDS system. Aberration-corrected HAADF-STEM images and atomic EDS mapping were obtained on the Thermo Fisher Themis Z. XPS experiments were conducted in the Thermo ESCALAB MK II X-ray photoelectron spectrometer with Al Kα as the excitation source. Quantitative analysis of material element composition was conducted by inductively coupled plasma-mass spectrometry (ICP-MS, Thermo Fisher, iCAP RQ). Samples were ground with graphite for XAFS analysis on the BL14W1 and BL20U beamline of the Shanghai Synchrotron Radiation Facility.

XPS depth characterizations

XPS depth profiling analysis was achieved by using synchrotron radiation X-ray as an excitation source and implemented at BL10B photoemission end stations in the National Synchrotron Radiation Laboratory. Probing depth was achieved by regulating the kinetic energy of the emitted photoelectrons of specific core electron energy level to the relative predefined value. The binding energies were calibrated by C 1*s* (284.6 eV) and the collecting energy step was 0.1 eV.

Stain mapping

Van Aert et al. proposed an efficacious model-based estimation algorithm to quantify the positions and intensities of atomic columns from atomic resolution (S)TEM images and developed a statSTEM software package using the MATLAB programming language. The atomic positions in the HAADF-STEM image of a $L1_0$-PtFe@$PtPd_{sub}$ NP were identified using statSTEM software. Based on these atomic position coordinates, we derived the spacing of the neighboring atomic columns and calculated the strain values compared to the theoretical values.

CO-adsorption diffuse reflectance infrared Fourier transform spectroscopy

CO-DRIFTS characterization was performed on a Nicolet iS10 spectrometer. After mixing and grinding the samples with KBr and loading them into an in-situ reaction cell (Praying Mantis Harrick), the samples were first treated in 10% O_2/Ar at 150 °C for 30 min and then reduced in 10% H_2/Ar at 150 °C for 30 min. Subsequently, the samples were continuously vented with Ar at a flow rate of 20 mL/min, cooled to 25 °C and a background spectrum was obtained until a stable baseline was achieved. Subsequently, a switch to 10% CO was made until the sample was saturated with adsorption. Next, the sample was switched back to Ar for purging and DRIFT spectra were collected until the CO gas-phase peak disappeared. Spectral acquisition parameters were as follows: 256 scans with a resolution of 4 cm^{-1}.

Electrochemical measurements (rotating disk electrode test)

Electrochemical ORR testing was conducted using a CHI700E electrochemical station and a Pine ASR rotator. The Pine ASR instrument was equipped with a glassy carbon electrode as the working electrode (0.196 cm^2), Pt sheet as the counter electrode, Ag/AgCl (saturated KCl) electrode as the reference electrode, and the electrolyte was 0.1 M $HClO_4$ solution (pH = 1.01 ± 0.03, determined from five independent measurements). 0.1 M $HClO_4$ electrolyte was prepared by diluting 2.16 mL high-purity concentrated $HClO_4$ (70–72%) with DI water in a 250 mL volumetric flask. The electrolyte was prepared immediately before use. The Ag/AgCl electrode was calibrated for a RHE with a Pt sheet in a high-purity H_2-saturated electrolyte. All catalyst inks were prepared by dispersing 1 mg of the as-prepared catalysts in a mixture containing 0.985 mL isopropanol and 15 μL Nafion® and ultrasonicating for 30–60 min to form a 1 mg/mL ink. 10–15 μL of ink was cast on the glassy carbon and dried under ambient conditions. The final loadings were about 10 μg cm^{-2} for $L1_0$-PtFe@Pt/C and $L1_0$-PtFe@PtM_{sub}/C electrocatalysts according to ICP-MS.

For electrochemical tests, CV curves were scanned in N_2-saturated 0.1 M $HClO_4$ from 0.05 to 1.2 V vs. RHE at a scan rate of 50 mV s^{-1} to obtain. Only when the CV curves reached a steady state could they be used for background subtraction and ECSA determination. And the ORR polarization curves, corrected for iR drop (E-iR), were carried out in O_2-saturated 0.1 M $HClO_4$ at 10 mV s^{-1}. ADT tests were performed by scanning between 0.6 and 1.0 V vs. RHE in O_2-saturated 0.1 M $HClO_4$ at 100 mV s^{-1}. The solution resistance was determined to be 19.7 ± 3.51 Ω by the CHI700E electrochemical station.

CO stripping measurement involved three processes: high-purity CO was first bubbled into a 0.1 M $HClO_4$ solution holding the potential at 0.05 V vs. RHE for 10 min, then pure N_2 was bubbled into the electrolyte for 10 min, and finally, the voltammetry curve was scanned from +0.05 to +1.15 V vs. RHE at a scanning rate of 50 mV s^{-1}.

All measured potentials were converted to the RHE using the Nernst equation:

$$E_{RHE} = E_{Ag/AgCl} + 0.197 + 0.0592 \times pH \quad (1)$$

Calculation methods for MA, SA, and ECSA

Firstly, the CV curve was obtained by scanning at a rate of 50 mV s^{-1} within the potential range of 0.0–1.2 V in a N_2-saturated 0.1 M $HClO_4$ solution. Subsequently, the ECSA was calculated by integrating the hydrogen adsorption peaks (approximately 0.05–0.4 V) on the CV curve to obtain the charge quantity (Q_H), with the assumption that the value for a monolayer of adsorbed hydrogen is 210 μC/cm^2. The specific equation is as follows:

$$ECSA = \frac{Q_H}{2.1 M_{Pt}} \quad (2)$$

Where M_{Pt} (μg_{Pt}) represents the Pt loading on the working electrode.

The kinetic currents (I_k) can be calculated using the Koutecký-Levich equation:

$$\frac{1}{I} = \frac{1}{I_k} + \frac{1}{I_d} \quad (3)$$

where I is the measured current and I_d is the diffusion-limited current. I_d can be determined using the Levich equation:

$$I_d = 0.62nFAD^{2/3}\upsilon^{-1/6}\omega^{1/2}C_{O_2} \quad (4)$$

where n is the number of electrons transferred, F is the Faraday constant (96485 C/mol), A is the geometric area of the working electrode (0.196 cm^2), D is the diffusion coefficient of oxygen in 0.1 M $HClO_4$ (1.93×10^{-5} cm^2/s), υ is the kinematic viscosity of the 0.1 M $HClO_4$ (1.01×10^{-2} cm^2/s), ω is the rotation rate, and C_{O2} is the concentration of oxygen molecules in 0.1 M $HClO_4$ (1.26×10^{-6} mol/cm^3).

The MA of the catalyst is calculated by normalizing the kinetic current at 0.9 V vs. RHE to the Pt loading (μg_{Pt}) on the working electrode.

$$MA = \frac{I_{k-0.9V}}{M_{Pt}} \quad (5)$$

The SA of the catalyst is obtained by dividing the MA by the ECSA.

$$SA = \frac{MA}{ECSA} \quad (6)$$

Fuel-cell measurements

The 30 mg $L1_0$-PtFe@$PtPd_{sub}$/C catalysts, and commercial 30 wt% Pt/(TEC10E30E) were mixed with 10 mL of water/isopropanol with a 1:1 ratio in a serum bottle. Nafion solution (Aquivion® D79-25BS Perfluorosulfonic Acid, 25%) was adapted as proton conductor and cross-linking agent. The mixture was ultrasonicated for 120 min to obtain a homogeneous ink. The concentration of all inks was controlled to be 3 $mg_{cat.}$ mL^{-1}. The optimized I/C ratio of ink was controlled to 0.6. The catalyst-coated-membrane (CCM) was prepared on GORE Nafion membrane (active area of 5 cm^2) with an ultrasonic spray equipment (SONO·TEK). The carbon paper (22BB SGL Carbon) with a 215 μm-thick microporous layer was used as a gas diffusion layer (GDL). The MEA contained five parts with two GDLs, two gaskets (140 μm), and the prepared CCM. The Pt loadings of all MEAs at cathode and anode were controlled to be 0.1 and 0.05 mg_{Pt} cm^{-2}, respectively.

Then the MEA was packaged in a single cell and tested in the 850e fuel cell test system (Scribner Associates, Inc.), with seven channel serpentine flow field. The cell pre-activation was performed before data collection as followed. As the cell and humidifiers to 80 °C, the cell voltage was swept from open circuit to 0.3 V under H_2–O_2 conditions

at 150 kPa_{abs} and 100% relative humidity (RH) with several cycles until the current density was stable. The MA was obtained from H_2–O_2 conditions (0.2/0.5 L min^{-1}) at 80 °C, 150 kPa_{abs} and 100% RH. The fuel cell was operated at 0.9 V_{iR}-correct for 15 min, and the MA was obtained from the average current density at the last 1 min. The H_2-air polarization curve was collected under 80 °C, 150 kPa_{abs} and 100% RH (or 94 °C, 250 kPa and 90% RH), with the H_2/air flow of 0.5/2 L min^{-1}. The accelerated stress test (AST) was adopted 30,000 cycles of square wave holding 3 s at voltage 0.6 V and then 3 s at voltage 0.95 V under 80 °C, 100 kPa_{abs} and 100% RH with H_2/N_2 flow of 0.2/0.075 L min^{-1}, according to DOE standards.

Quasi-in-situ identical location-(S)TEM (IL-STEM) measurements

The IL-STEM experimental procedure is described in four sequential steps:

1. Structural characterization of as-prepared catalysts at identical locations

   Firstly, the catalyst ink was deposited onto Au TEM grids selected for the chemical inertness of Au. Initial STEM characterization focused on nanoparticles in the central region of the Au grid—an area with distinct morphological features that enabled precise relocation for comparative post-reaction analysis. Following atomic-resolution HAADF-STEM imaging of target nanoparticles, a series of multi-magnification images were acquired to establish precise positional references.
2. Fabrication of the working electrode assembly for IL-STEM characterization

   Firstly, we modified the conventional working electrode by affixing a helical cap on the glassy carbon electrode side, the cap featuring a central aperture with a diameter slightly smaller than that of the Au grid, thereby ensuring effective electrode-electrolyte interfacial contact. Subsequently, the Au grid dropped with catalysts was positioned at the center of the glassy carbon electrode with the catalyst-coated side facing outward, and securely immobilized by tightening the helical cap.
3. Electrochemical cycling tests

   The IL-STEM electrochemical cycling protocol mirrored standard RDE methodologies. After the working electrode integrated the Au grid was installed in a Pine Research RDE holder, ADTs were performed. Notably, despite the ultralow catalyst loading on the IL-STEM working electrode, the system maintained characteristic CV profiles.
4. Structural characterization of catalysts at identical locations in the desired reaction stage

Upon reaching the desired reaction stage, the Au grid is removed from the reaction system and transferred to the TEM. After the central region of the Au grid was found under the low-magnification TEM imaging, precisely relocating the target catalyst nanoparticles by using pre-acquired multi-scale reference images, and performing the HAADF-STEM imaging.

The above process can be repeated at different reaction stages in order to study the structural evolution of the catalyst under electrocatalytic reaction conditions.

Theoretical calculations

All the density functional theory calculations were conducted using the Vienna ab initio Simulation Package with the projector-augmented wave pseudopotentials. The generalized gradient approximation with the Perdew–Burke–Ernzerhof function was used to describe the exchange-correlation energy. The plane-wave energy cutoff is 500 eV, and the convergence criterion of the electronic self-consistent iteration was set to be 10^{-6} eV. The structures were relaxed, and the convergence criterion of the force on each atom is 0.01 eV $Å^{-1}$. The Monkhorst-Pack 3 × 3 × 1 k-point grid was used to sample the Brillouin zone.

The slab model of $L1_0$-PtFe@Pt(Pd_{sub}) was constructed based on the Pt (111) surface model in a 4 × 4 in-plane supercell. The vacuum layer was set to be 15 Å to ensure the slabs were separated.

The elementary steps in the four-electron ORR occurs are believed to involve surface-adsorbed OOH*, O*, and OH* species, as follows:

$$O_2\,(g) + * + H^+ + e^- \rightarrow OOH^* \tag{7}$$

$$OOH^* + H^+ + e^- \rightarrow H_2O + O^* \tag{8}$$

$$O^* + H^+ + e^- \rightarrow OH^* \tag{9}$$

$$OH^* + H^+ + e^- \rightarrow * + H_2O \tag{10}$$

The Gibbs free energy change (ΔG) for each adsorbate can be calculated by employing the CHE model developed by Nørskov et al.:

$$\Delta G_{ads} = \Delta E_{ads} + \Delta ZPE_{ads} - T\Delta S_{ads} + \Delta G_U + \Delta G_{pH} \tag{11}$$

$$\Delta G_{pH} = T \times k_B \times pH\ln 10 \tag{12}$$

where ΔE is the adsorption energy obtained from DFT calculation, ΔZPE is the zero-point energy correction, T is the temperature (298.15 K), ΔS is the entropy change. U is the implemented potential, ΔG_{pH} represents the free energy correction of the pH, k_B is the Boltzmann constant.

The surface energies (E_{surf}) of all the relevant surfaces were calculated by the following formula:

$$E_{surf} = (E_{slab} - nE_{bulk})/2A \tag{13}$$

where E_{slab} and E_{bulk} are the total energies of the slab and a bulk unit, respectively; n represents the number of atoms in the slab, and A is the exposed surface area of one side of the slab.

The formation energy (E_f) was defined as follows:

$$E_f = E_{vacancy} - E_{pristine} - \mu_{Pd} \tag{14}$$

where $E_{vacancy}$ and $E_{pristine}$ are the total energies of structures with and without a vacancy, respectively, and μ_{Pd} is the chemical potential of Pd.

Data availability

The experiment data that support the findings of this study are provided in the Source Data file. The atomic coordinates of the optimized $L1_0$-PtFe@$PtPd_{sub}$ and $L1_0$-PtFe@Pt models are provided as Supplementary Data 1 and 2, respectively. Source data and Supplementary Data are provided with this paper. Source data are provided with this paper.

References

1. Tao, F. & Salmeron, M. Surface restructuring and predictive design of heterogeneous catalysts. *Science* **386**, eadq0102 (2024).
2. Ledentu, V. et al. Heterogeneous catalysis through subsurface sites. *J. Am. Chem. Soc.* **122**, 1796–1801 (2000).
3. Li, P. et al. Manipulation of oxygen species on an antimony-modified copper surface to tune the product selectivity in CO_2 electroreduction. *J. Am. Chem. Soc.* **146**, 26525–26533 (2024).
4. Jalil, A. et al. Nickel promotes selective ethylene epoxidation on silver. *Science* **387**, 869–873 (2025).

5. Nam, D.-H. et al. Molecular enhancement of heterogeneous CO_2 reduction. *Nat. Mater.* **19**, 266–276 (2020).
6. Chen, S. et al. Selective CO_2 reduction to ethylene mediated by adaptive small-molecule engineering of copper-based electrocatalysts. *Angew. Chem. Int. Ed.* **62**, e202315621 (2023).
7. Zhao, K. et al. A molecular design strategy to enhance hydrogen evolution on platinum electrocatalysts. *Nat. Energy* **10**, 725–736 (2025).
8. Zhao, Z. et al. Graphene-nanopocket-encaged PtCo nanocatalysts for highly durable fuel cell operation under demanding ultralow-Pt-loading conditions. *Nat. Nanotech.* **17**, 968–975 (2022).
9. Ma, X. et al. Carbonate shell regulates CuO surface reconstruction for enhanced CO_2 electroreduction. *Nat. Synth.* **4**, 53–66 (2025).
10. Cao, X. et al. Sandwiching intermetallic Pt_3Fe and ionomer with porous N-doped carbon layers for oxygen reduction reaction. *Nat. Commun.* **16**, 2851 (2025).
11. Li, Y. et al. Accelerated selective electrooxidation of ethylene glycol and inhibition of C-C dissociation facilitated by surficial oxidation on hollowed PtAg nanostructures via in situ dynamic evolution. *JACS Au* **5**, 714–726 (2025).
12. Peng, B. et al. Embedded oxide clusters stabilize sub-2 nm Pt nanoparticles for highly durable fuel cells. *Nat. Catal.* **7**, 818–828 (2024).
13. Tao, F. et al. Reaction-driven restructuring of Rh-Pd and Pt-Pd core-shell nanoparticles. *Science* **322**, 932–934 (2008).
14. Song, Y. et al. Bimetallic synergy from a reaction-driven metal oxide-metal interface of Pt-Co bimetallic nanoparticles. *ACS Catal.* **13**, 13777–13785 (2023).
15. Mu, R. et al. Synergetic effect of surface and subsurface Ni Species at Pt-Ni bimetallic catalysts for CO Oxidation. *J. Am. Chem. Soc.* **133**, 1978–1986 (2011).
16. Lin, Y. et al. Optimizing surface active sites via burying single atom into subsurface lattice for boosted methanol electrooxidation. *Nat. Commun.* **16**, 286 (2025).
17. Vitale-Sullivan, M. & Stoerzinger, K. A. Interplay of surface and subsurface contributions in electrocatalysis. *Curr. Opin. Electrochem.* **39**, 101252 (2023).
18. Teschner, D. et al. The roles of subsurface carbon and hydrogen in palladium-catalyzed alkyne hydrogenation. *Science* **320**, 86–89 (2008).
19. Jin, G. et al. Heteroepitaxial van der Waals semiconductor superlattices. *Nat. Nanotech.* **16**, 1092–1098 (2021).
20. Stephens, I. E. L. et al. Tuning the activity of Pt(111) for oxygen electroreduction by subsurface alloying. *J. Am. Chem. Soc.* **133**, 5485–5491 (2011).
21. Zhao, X. et al. Engineering covalently bonded 2D layered materials by self-intercalation. *Nature* **581**, 171–177 (2020).
22. Derouin, J. et al. Thermally selective formation of subsurface oxygen in Ag(111) and consequent surface structure. *ACS Catal.* **6**, 4640–4646 (2016).
23. Lu, J. Atomic lego catalysts synthesized by atomic layer deposition. *Acc. Mater. Res.* **3**, 358–368 (2022).
24. Guan, Q. et al. Bimetallic monolayer catalyst breaks the activity-selectivity trade-off on metal particle size for efficient chemoselective hydrogenations. *Nat. Catal.* **4**, 840–849 (2021).
25. Jin, S. et al. Atom-by-atom design of Cu/ZrOx clusters on MgO for CO_2 hydrogenation using liquid-phase atomic layer deposition. *Nat. Catal.* **7**, 1199–1212 (2024).
26. Yang, L. et al. Cation exchange in colloidal transition metal nitride nanocrystals. *J. Am. Chem. Soc.* **146**, 12556–12564 (2024).
27. Wang, Z. et al. Tailored lattice compressive strain of Pt-Skins by the $L1_2$-Pt_3M intermetallic core for highly efficient oxygen reduction. *Adv. Mater.* **35**, 2301310 (2023).
28. Shi, Y. et al. Noble-metal nanocrystals with controlled shapes for catalytic and electrocatalytic applications. *Chem. Rev.* **121**, 649–735 (2021).
29. Zhao, M. et al. Hollow metal nanocrystals with ultrathin, porous walls and well-controlled surface structures. *Adv. Mater.* **30**, 1801956 (2018).
30. Tran, R. et al. Surface energies of elemental crystals. *Sci. Data* **3**, 160080 (2016).
31. Huang, X. et al. High-performance transition metal-doped Pt_3Ni octahedra for oxygen reduction reaction. *Science* **348**, 1230–1234 (2015).
32. Luo, H. et al. Amorphous MoO with high oxophilicity interfaced with PtMo alloy nanoparticles boosts anti-CO hydrogen electrocatalysis. *Adv. Mater.* **35**, 2211854 (2023).
33. Ramirez Caballero, G. E. & Balbuena, P. B. Surface segregation phenomena in Pt-Pd nanoparticles: dependence on nanocluster size. *Mol. Simul.* **32**, 297–303 (2006).
34. Shao, R. Y. et al. Promoting ordering degree of intermetallic fuel cell catalysts by low-melting-point metal doping. *Nat. Commun.* **14**, 5896 (2023).
35. Hu, J. et al. Unique applications of carbon materials in infrared stealth: a review. *Chem. Eng. J.* **452**, 139147 (2023).
36. Aleksandrov, H. A. et al. Can the state of platinum species be unambiguously determined by the stretching frequency of an adsorbed CO probe molecule? *Phys. Chem. Chem. Phys.* **18**, 22108–22121 (2016).
37. Bazin, P. et al. FT-IR study of CO adsorption on Pt/CeO_2: characterisation and structural rearrangement of small Pt particles. *Phys. Chem. Chem. Phys.* **7**, 187–194 (2005).
38. De Backer, A. et al. StatSTEM: an efficient approach for accurate and precise model-based quantification of atomic resolution electron microscopy images. *Ultramicroscopy* **171**, 104–116 (2016).
39. Xie, M. et al. Pt-Co@Pt octahedral nanocrystals: enhancing their activity and durability toward oxygen reduction with an intermetallic core and an ultrathin shell. *J. Am. Chem. Soc.* **143**, 8509–8518 (2021).
40. Liu, X. et al. Introducing electron buffers into intermetallic Pt alloys against surface polarization for high-performing fuel cells *J. Am. Chem. Soc.* **146**, 2033–2042 (2024).
41. Yang, L. et al. Rare earth evoked subsurface oxygen species in platinum alloy catalysts enable durable fuel cells. *Angew. Chem. Int. Ed.* **63**, e202315119 (2024).
42. Wang, Z. et al. Strain engineering of Pt-based electrocatalysts for oxygen reaction reduction. *Front. Energy* **18**, 241–262 (2024).
43. Office of Energy Efficiency & Renewable Energy. Energy. gov. 2016. https://www.energy.gov/eere/.
44. Beermann, V. et al. Real-time imaging of activation and degradation of carbon supported octahedral Pt-Ni alloy fuel cell catalysts at the nanoscale using in situ electrochemical liquid cell STEM. *Energy Environ. Sci.* **12**, 2476–2485 (2019).
45. Huang, H. & Russell, A. E. Approaches to achieve surface sensitivity in the in situ XAS of electrocatalysts. *Curr. Opin. Electrochem.* **27**, 100681 (2021).
46. Ortiz Peña, N. et al. Morphological and structural evolution of Co_3O_4 nanoparticles revealed by in situ electrochemical transmission electron microscopy during electrocatalytic water oxidation. *ACS Nano* **13**, 11372–11381 (2019).
47. Hrnjic, A. et al. Observing, tracking and analysing electrochemically induced atomic-scale structural changes of an individual Pt-Co nanoparticle as a fuel cell electrocatalyst by combining modified floating electrode and identical location electron microscopy. *Electrochim. Acta* **388**, 138513 (2021).
48. Zhi-Peng, W. et al. Applications of in situ electron microscopy in oxygen electrocatalysis. *Microstructures* **2**, 2022002 (2022).

Acknowledgements
This work was supported by the National Natural Science Foundation of China (52122212, Y.L.; 12274391. Y.L.; 22321001, C.W. and Y.L.; 12404225, X.H.; Grant nos. 22525013, C.W.), the Youth Innovation Promotion Association of CAS (2020458, Y.L.), the Key Research Program of Frontier Sciences, CAS (ZDBS-LY-SLH003, Y.L.), CAS Project for Young Scientists in Basic Research (YSBR-070, C.W.), the National Key Research and Development Program of China (2022YFB3807602, Y.L.; 2022YFA1203600, C.W.), China Postdoctoral Science Foundation (2023M743348 and 2024T170888, X.H.), Postdoctoral Fellowship Program of CPSF (GZC20232511, X.H.) and the University Synergy Innovation Program of Anhui Province (GXXT-2022-007, H.D.). The calculations were performed on the Supercomputing Center of the University of Science and Technology of China. We thank the photoemission end stations MCD-A, MCD-B, BL10B, BL01B in the National Synchrotron Radiation Laboratory (NSRL) and BL14W1, BL20U in the Shanghai Synchrotron Radiation Facility (SSRF) for help in characterizations.

Author contributions
Y.L. and C.W. conceived the idea and co-wrote the paper. X.T., S.X., and X.H. carried out the sample synthesis, characterization, and electrochemical performance measurement. Y.Z. calculated the DFT calculation. L.X. analyzed the XAS results. Y.X. drew the schematic diagram. H.D., R.G., and M.M. discussed with results and helped with the modification of the paper.

Competing interests
The authors declare no competing interests.

Additional information
Supplementary information The online version contains supplementary material available at https://doi.org/10.1038/s41467-025-67296-1.

Correspondence and requests for materials should be addressed to Xiao Han, Changzheng Wu or Yue Lin.

Peer review information *Nature Communications* thanks Qing Li and the other anonymous reviewer(s) for their contribution to the peer review of this work. A peer review file is available.